A Modified Factorized Geometrical Autofocus Method for Wide Angle SAR

Han Li, Zhiyong Suo, Chengxin Zheng, Zhenfang Li, and Bingji Zhao

***Abstract*—Wide-Angle (WA) synthetic aperture radar (SAR) has shown remarkable performance in high-resolution mapping, and its mostly used imaging algorithm, fast factorized back projection (FFBP), is efficient, robust, and of low computational complexity. However, trajectory deviations and the system calibration error, introduced by low measurement accuracy, dramatically degrade FFBP's performance. This article proposes the modified factorized geometrical autofocus (MFGA) method for WA-SAR to address the above problems in FFBP. MFGA implements the phase gradient algorithm on defocus subimages at first. Then, a factorized geometrical error hypothesis between subimages is proposed. And the corresponding defocus factors are classified as three independent parts: image distortion, spectrum migration, and phase error. To deal with those problems, MFGA introduces image registration techniques and a maximum sharpness method to calibrate image distortion and phase error. Moreover, in MFGA, based on minimum entropy and least square method, a Doppler spectrum migration correction algorithm is proposed to correct spectrum migration. In the FFBP chain, MFGA is used on subimages refocus and fusion until obtaining a full-resolution image. In our experiments, we compared MFGA and other time-domain autofocus algorithms using simulated data and real data obtained by helicopter and airship with false trajectory and system calibration parameters. The results show that MFGA performs better in terms of the peak to side-lobe ratio, the azimuth resolution, the refocused images' entropy, and processing time consumption. The better performance demonstrates MFGA's advantages in addressing trajectory deviations and the system calibration error for WA-SAR.**

***Index Terms*—Autofocus, fast factorized back projection, phase gradient algorithm, spectrum migration, system calibration error, wide angle synthetic aperture radar.**

I. Introduction

SYNTHETIC aperture radar (SAR) is a powerful and widely used microwave remote sensing system under an all-time and all-weather environment [1], [2]. As a new SAR system, the employment of wide-angle SAR (WA-SAR) can obtain higher resolution and more anisotropic scattering information by imaging the same scene from wide aspect angle which useful in target recognition [3]–[5].

Until now, there are mainly two different kinds of SAR imaging methods. One is based on specific signal model, called frequency domain imaging algorithm [6]–[8]. Frequency domain imaging algorithms have good computational performance if the motion state (actually the antenna phase center, APC) of the radar platform conforms to the method hypothesis, e.g., the radar platform moves at a constant velocity. Another kind of image method is the back-projection algorithm (BPA), called time domain method [9], which is convenient and suitable for all kinds of SAR systems with accurate APC positions. However, its disadvantage is the high computation complexity of $O(N^3)$, where N represents the azimuth sampling number. Therefore, many improved BPA have been proposed to reduce the computation complexity [10], [11]. The fast factorized back projection (FFBP) can reduce the computation complexity to $O(N^2\log_2 N)$. And its validity has been investigated by processing real data successfully in [12] and [13]. In [14], FFBP has been successfully expanded on stripmap SAR data processing.

Similar to all time domain imaging algorithms, the performance of FFBP is seriously affected by the system parameters measurement errors. One is the APC accuracy. Generally, some instruments, such as the global positioning system (GPS) and inertial measurement unit (IMU) [15], [16] are used to measure the motion statement of the radar platform. The measurement accuracy of such devices, however, normally not meets the requirement of WA-SAR imaging. Another is system calibration error. The range calibration (RC) error will cause range cell migration correction (RCMC) error and affect azimuth compression.

Autofocus methods are the most common solution to rebuilt well-focused image. Most of them are based on the frequency domain, such as phase gradient algorithm (PGA) [17]–[19], map drift (MD) [19]–[21], and so on. Combing with MD, an autofocused image algorithm for FFBP, MAMD [22], applies MD to estimate several residual frequency rate of several BP subimages to fit high order equation of phase error to accomplish refocus. Unfortunately, the precondition of MAMD is that the RCMC is well compensated [22]. That is to say that MAMD is invalid if the wrong RCMC caused by the system calibration error and large APC error. Moreover, PGA and MD cannot be directly applied to squint SAR or WA-SAR [23]. Based on FBP and FFBP, Garber indicates that PGA is useful if the images were focused on virtual polar coordinates system [24]. However, most of them are failure in WA-SAR refocus because of the limitation

Manuscript received August 12, 2020; revised October 10, 2020; accepted December 14, 2020. Date of publication December 17, 2020; date of current version January 8, 2021. This work was supported in part by the National Natural Science Foundation of China under Grant 61671355. *(Corresponding author: Zhiyong Suo.)*

Han Li, Zhiyong Suo, and Zhenfang Li are with the National Laboratory of Radar Signal Processing, Xidian University, Xi'an 710071, China (e-mail: lihwork@163.com; zysuo@xidian.edu.cn; lzf@xidian.edu.cn).

Chengxin Zheng is with the Shanghai Radio Equipment Research Institute, Shanghai 200090, China (e-mail: zhengchx6017@163.com).

Bingji Zhao is with the Beijing Institute of Spacecraft System Engineering in CAST, Beijing 100094, China (e-mail: zachary_zbj@163.com).

Digital Object Identifier 10.1109/JSTARS.2020.3045477

of azimuth angle width. Thus, combined with PGA, a method called factorized geometrical autofocus (FGA) is proposed in [25]–[27]. In FGA, several well-focused subimages by PGA are obtained. Then six parameters are used to describe the geometry error between subimages, and searched for all of the subimages to finish subimage fusion. The disadvantages of PGA include the low geometric parameters estimation accuracy and huge computation cost. Moreover, six parameters are insufficient in the relative geometry description of WA-SAR with multiple measurement errors, such as the system calibration error has not been considered. Based on image quality evaluation criterion, there are other kinds of BPA autofocus methods that have been proposed [30]–[35]. The processing results, which are given by the authors, show that it is effective in using the image quality criterion to evaluate the SAR image performance. Nevertheless, the tremendous computational complexity, large iteration time, and huge storage limit its application. Besides that, RCMC error is ignored in those algorithms. Recently, a new kind of autofocus methods [28], [29] aiming at recovering the high precise 3-D APC are proposed. The disadvantage of those algorithms is that the trajectory inversion accuracy is limited by the phase estimated algorithm which is invalidated under the influence of RC error. In conclusion, for WA-SAR, the traditional autofocus methods face multiple limitations, such as tremendous computational complexity, azimuth angle width restriction, and system calibration error. Moreover, the most important defocus factor, RCMC error, has not been fully considered before.

To overcome those limitations, a modified FGA (MFGA) for WA-SAR with system calibration error is proposed in this article. The arrangement of this article is as follows. In Section II, the principle of FFBP is introduced. And the influence of system calibration on FFBP imaging is analyzed. In Section III, MFGA is put forward. In the first step of MFGA, PGA is implemented on subdatasets to obtain well-focused subimages. Then, a factorized geometrical error hypothesis between subimages is proposed. Different from traditional FGA, system calibration error is introduced to the geometrical error. Moreover, unlike with the search strategy of geometrical error of traditional FGA [26], the strategy of MFGA is to divide the defocus factors caused by geometrical error into several categories and calibrated them independently. Integrated into the FFBP chain, one full-resolution focused image is finally obtained by MFGA. By utilizing PGA and base-2 recursion configuration, the computational complexity will be alleviated greatly compared to the traditional FFBP autofocus methods. Furthermore, the complexity and low efficient searching of traditional FGA can also be avoided. In Section IV, simulated and real data experiments on the WA-SAR system carried by helicopter and airship are put forward to address the effectiveness of MFGA.

II. Exposition of FFBP

A. Principle of FFBP

Compared to BPA, FFBP has much less computational complexity. The principle model of FFBP is shown in Fig. 1. The radar echoes are first divided by FFBP into subaperture datasets. And then the subimages are rebuilt in different polar coordinates systems with low and appropriate angular sampling rates by BPA.

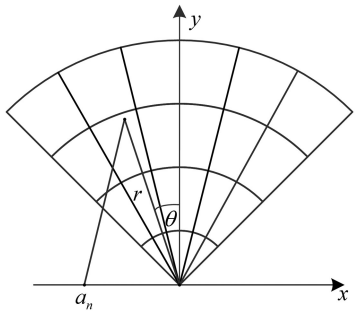

Fig. 1. Implementation of FFBP.

The image results $I_m^0(r,\theta)$ of the subaperture in the first level is expressed as follows:

$$I_m^0(r,\theta) = \int_l s(a,r)\, \mathrm{e}^{j\frac{4\pi r}{\lambda}} da \quad m = 1, 2, \ldots, M \tag{1}$$

where (r,θ) represent the range position and angular position of pixels in the polar coordinates systems corresponding to the current processing subaperture image; m means the mth subimage, $M$is a number with power of 2; $s(a,r)$ is the range compressed echo; a is the azimuth sampling position; l is the integral interval of synthetic aperture of each subimage. In the second level of SAR imaging, the images of the first level are resampled into new polar coordinates (r',θ'). Assumed that the moving trajectory of radar platform is an ideal straight line, the subimages $I_m^{k+1}(r',\theta')$of the $(k+1)$th level can be obtained as follows:

$$I_m^{k+1}(r',\theta') = I_{2m-1}^k(r',\theta') + I_{2m}^k(r',\theta'). \tag{2}$$

Repeating (2) until one full-resolution image is left. The computational complexity is proportional to $2N^2\log_2 N$ (for N sample number within an $N \times N$ image).

B. FFBP With System Calibration Error

As we all know, the performance of FFBP is seriously affected by APC accuracy. Moreover, system calibration error, includes RC error and azimuth calibration error, could also cause defocus. RC error is caused by the system time delay error. Assuming that the radar track is an ideally straight line, the sampling positions, shown in Fig. 2, is expressed as$a_n, n = 1, 2 \ldots . N$. The slant range r_n betweena_n and gridding position P_0 is formulated as follows:

$$r_n = \|a_n - p\|_2, n = 1, 2, 3 \ldots . N \tag{3}$$

where $\|\cdot\|_2$ is 2-norm function. If the RC is accurate, the geometrical projection of the recorded echo is circle Θ_n , whose radius equals to $r_n$and the center is a_n. As shown in Fig. 2, all of Θ_n are intersected at P_0. The target is well-focused atP_0. However, because of the RC error, the ideal nearest slant range cannot be accurately achieved. Affected by the nearest slant range errorδr , the projected circle is changed from Θ_n to $\tilde{\Theta}_n$, whose radius is $r_n + \delta r$. $\tilde{\Theta}_n$ is tangent to circle $\Theta^{\dagger}$, whose

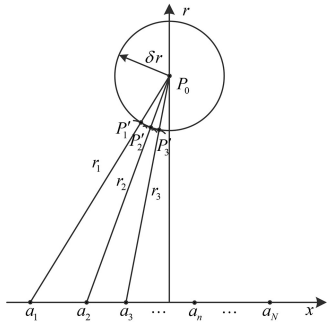

Fig. 2. Effect of range calibration error on SAR imaging.

radius is δr and the corresponding center is P_0. The point of intersection between $\tilde{\Theta}_n$ and $\Theta^{\dagger}$ is P'_n.

To explain the influence of RC error on FFBP, the energy distribution of imaging result is analyzed. Considered thata_2 is close enough to a_1, then $\tilde{\Theta}_2$and $\tilde{\Theta}_1$ are intersected at P'_1. Meanwhile, closely a_2 and a_3 represented that $\tilde{\Theta}_2$ and$\tilde{\Theta}_3$are intersected at P'_3. Therefore, the energy of P_0 will spread along $\Theta^{\dagger}$ and the image result of BPA is defocused. Meanwhile, the RCMC of $P_0$is inaccurate. For example, 50 m range calibration error with 10° squint angle will bring maximum 8.682 m azimuth energy distribution and 0.7596 m related RCMC error.

Azimuth calibration error is caused by the time synchronous error between the navigation instrument and the radar system. Normally, the time scale of radar and IMU should be synchronous to provide accurate APC to echo. Under the azimuth calibration error, the actual outputs of APC positions are shifted, which will lead to the projection geometry error and image defocus.

III. Proposed Autofocus Method for FFBP

As described in the previews section, the performance of FFBP is mainly decided by APC measurement error and system calibration error. Nonconstant motion error leads to bring extra high order azimuth varied phase to the data and cause FFBP filter mismatch. System calibration error results in RCMC error and azimuth defocus. To obtain well-focused image result, a MFGA method for WA-SAR with system calibration error is proposed. The flowchart of the MFGA is shown in Fig. 3. The key procedures are as follows.

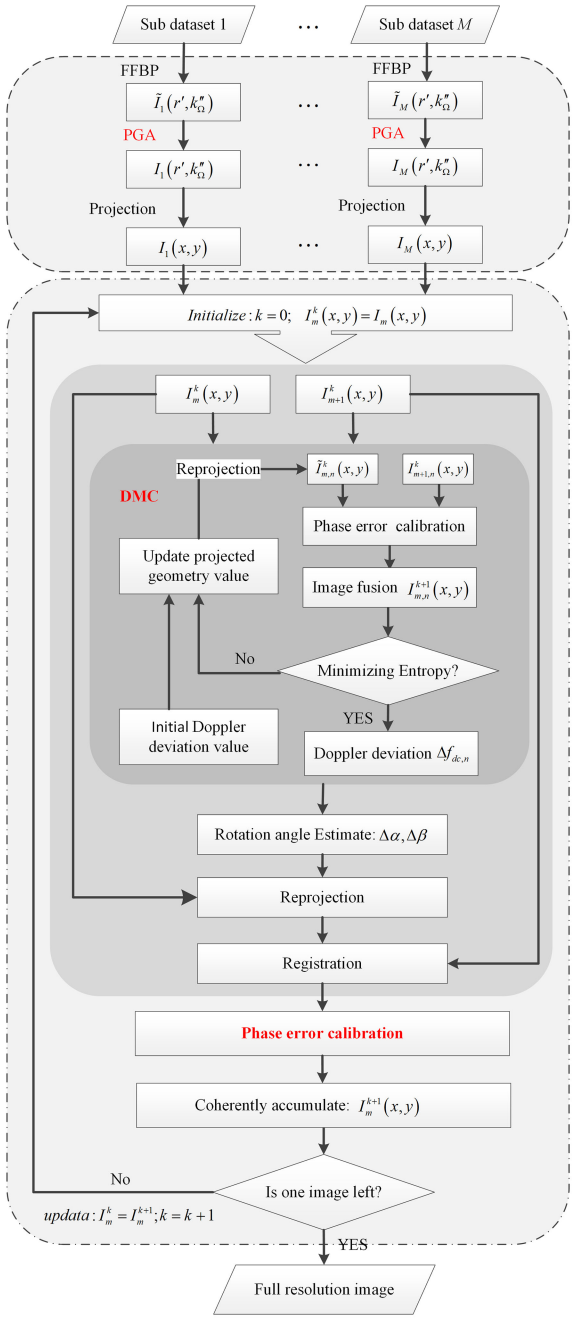

Fig. 3. Flowchart of MFGA.

A. PGA for Subimages

The basic hypothesis of PGA is that the residual range cell migration (RCM) is ignorable. However, influenced by range calibration error δr and WA, the residual RCM especially for WA-SAR, is non-negligible. Thus, to reduce the influence of RCMC error, subimages are refocused first. The beamwidth $\Delta\xi$ of subimage should follow the restriction that the residual RCM is smaller than half of the range sampling interval r_{cell}. The formulation is shown as follows:

$$\sqrt{(r+\delta r)^2 - 2(r+\delta r)\delta r\cos(\Delta\xi) + (\delta r)^2} - r \le r_{\text{cell}}/2 \Rightarrow \Delta\xi \le \sqrt{r_{\text{cell}}/(2\delta r)}. \tag{4}$$

Under the restriction of (4) and based on [24], PGA is used in defocused subimages which are imaged on virtual polar coordinates (r, Ω) by FFBP. r is the slant range, $\Omega = \sin(\theta)$, θ is the squinted angle. The point spread function of imaging

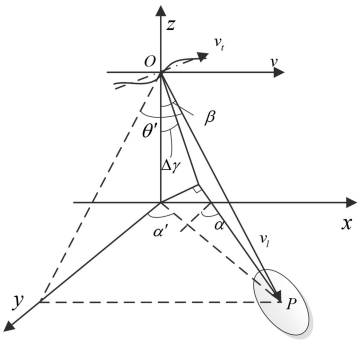

Fig. 4. Diagram of projective geometry.

result after PGA can be written as follows:

$$I\left(r,k_\Omega\right)=2L\ \mathrm{sinc}(k_\Omega vt)\mathrm{sinc}(r)\exp\left(-j\frac{4\pi}{\lambda}\Delta r\right) \tag{5}$$

where $k_\Omega=4\pi(\Omega-\Omega_p)/\lambda$ is the wave number, λ is the wave length; $L$is the synthetic aperture length; $\mathrm{sinc}(\cdot)$is the sinc function, and $\Delta r$is the interval of r.

Then, the well-focused subimages are projected into a unified imaging grid (the horizontal plane, xy-plane) for further image fusion. The projective geometry is shown in Fig. 4. The projection of (5) in xy-plane can be rewritten as

$$\begin{aligned}I\left(x,y\right)=&2L\mathrm{sinc}(r-r_p)\mathrm{sinc}(k_\Omega vt)\cdot\exp\left(-j\tfrac{4\pi}{\lambda}r_p\right)\\&\cdot\exp\left\{-j\tfrac{4\pi}{\lambda}\left[\Delta x\sin\left(\theta\right)+\Delta y\sin(\beta)\left(\cos\left(\theta\right)-1\right)\right]\right\}\end{aligned} \tag{6}$$

where θ is the included angle between LOS and axis x, $\beta$is the look-down angle, and $\Delta x$and $\Delta y$are the sampling interval of (x,y), respectively. It can be seen from (6) that the first term represents the amplitude. The phase $\theta_{in}=-4\pi r_p/\lambda$ of the first exponential term represents the interferometric phase which demonstrates the geometric relationship between target and trajectory. The last exponential term represents the spectrum characters that the Doppler centroid $f_{\mathrm{dc}}=2v\sin(\theta)/\lambda$ which is decided by θ , the frequency centroid $f_y=2v\sin(\beta)(\cos(\theta)-1)/\lambda$ in the ground range. Noted that the imaging result still can be formulated as (6) when the range compressed data directly focused in the xy plane.

B. Modified Factorized Geometrical Autofocus

However, affected by the track deviation and system calibration errors, the expression of (6) is inaccurate. In [26], Torgrimsson *et al*. put forward FGA which uses six parameters to describe the geometry error and search all the parameters based on the maximum intensity correlation criterion. However, for high-resolution mapping, the huge elapse time limits its implementation. Besides that, the influence of system calibration error (especially the range calibration error) and the possibility of interaction between the parameters have not been considered.

Thus, in this article, a MFGA is proposed. Based on the base-2 image merging principle of FFBP, the minimum unit (two adjacent subimages, I_m^0 and I_{m+1}^0) is processed. Presuming the projective geometry of I_{m+1}^0 is correct. By reducing the influence of the azimuth time calibration error into space angle error and trajectory error, the geometric errors hypothesis of I_m^0 are modified and expressed in the following quantities.

1) Track rotation angle (yaw angle: $\Delta\alpha$; pitch angle: $\Delta\gamma$) due to azimuth calibration and track measured error.
2) Space position error $(\Delta x,\Delta y,\Delta z)$ caused by azimuth calibration error and track measured error.
3) Range calibration error δr.

Then, (6) is changed to

$$\begin{aligned}I_m^0\left(x',y'\right)=&2L\ \mathrm{sinc}(r'-r_p)\mathrm{sinc}(k_\Omega vt)\\&\cdot\exp\left\{-j2\pi(f'_{\mathrm{dc}}t_x+{f'}_y t_y)-j{\theta'}_{in}\right\}\end{aligned} \tag{7}$$

where the parameters marked by " ' " are the corresponding parameters which are affected by geometric error, $f'_{\mathrm{dc}}=2v\sin(\theta')/\lambda$ is the new Doppler centroid, $f'_y$is the frequency centroid of ground range, and $t_x$and $t_y$are the sampling time of imaging grid. Compared (6) with (7), the influences of geometric error is divided as: image distortion (x',y'), spectrum migration $\Delta f_{\mathrm{dc}}=f_{\mathrm{dc}}-f'_{\mathrm{dc}}$, and phase error $\theta'_{in}=4\pi{r'}_p/\lambda$.

1) Image Distortion Calibration: Based on Fig. 4, the projected coordinates of I_m^0 in (7) can be written by

$$\begin{cases}x'=r'\sin(\theta')+{x'}_{\mathrm{ref}}\\y'=\sqrt{{r'}^2\cos^2(\theta')-{H'}_{\mathrm{ref}}{}^2}+{y'}_{\mathrm{ref}}\end{cases} \tag{8}$$

where $(x'_{\mathrm{ref}},y'_{\mathrm{ref}},H'_{\mathrm{ref}})$ are the coordinates of the reference point o of I_m^0. Based on the assumption, all the parameters on the right-hand side of (8) are inaccurate and result in image distortion of I_m^0. The target's energy is projected into different coordinates which will influence further image fusion. Thus, in MFGA, the image distortion between subimages is calibrated at first. However, finding all the parameters on the right-hand side of the equation is unrealistic. As an alternative solution, image registration methods [36] which based on the intensity correlation of the images are introduced to calibrate the image distortion between subimages. This procedure contains two steps.

Step 1 is coarse registration. During this step, $I_m^0(x',y')$ is resampled into I_{m+1}^0 , and accuracy of one pixel is reached. In step 2, fine image registration, such as the maximum correlation method, is utilized on the result obtained in step 1. The registration accuracy is up to 0.1 pixel of the azimuth resolution of subimages.

By utilizing fine image registration, the images' deformation caused can be corrected. The imaging result is optimized to

$$\tilde{I}_m^0\left(x,y\right)=\left|I_m^0\left(x,y\right)\right|\exp\left\{-j2\pi(f'_{\mathrm{dc}}t_x+{f'}_y t_y)-j{\theta'}_{in}\right\} \tag{9}$$

where $I_m^0(x,y)$is the ideal imaging result. Registration can calibrate the image distortion and make sure the energy of the target spread in the same coordinates.

2) Doppler Spectrum Migration Calibration: According to Fig. 4, affected by track rotation angle $(\Delta\alpha,\Delta\gamma)$, the vector of trajectory $\vec{v}_t$ and LOS $\vec{v}_l$ can be expressed as

$$\begin{cases}\vec{v}_t=[\cos(\Delta\alpha)\cos(\Delta\gamma),-\sin(\Delta\alpha)\cos(\Delta\gamma),\sin(\Delta\gamma)]\\\vec{v}_l=[\sin(\alpha')\sin(\beta),\cos(\alpha')\sin(\beta),-\cos(\beta)]\end{cases} \tag{10}$$

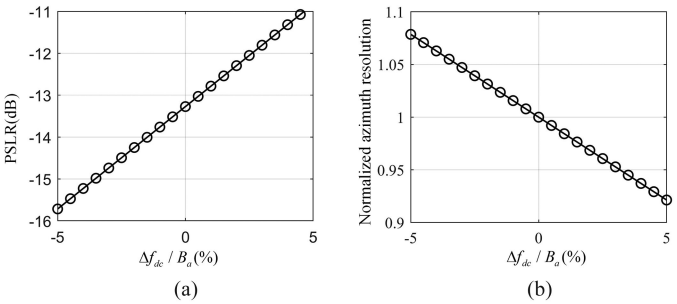

Fig. 5. (a) PSLR and (b) normalized azimuth resolution corresponding to $\Delta f_{\mathrm{dc}}/B_a$.

where β is the look-down angle of the target and $\alpha'$is the azimuth angle. The included angle between $\vec{v}_t$and $\vec{v}_l$ identically equals to $\pi/2-\theta$. Therefore, the relationship between $\vec{v}_t$ and $\vec{v}_l$ is given by

$$\sin(\theta)=\frac{\vec{v}_t\vec{v}_l^{\mathrm{T}}}{\|\vec{v}_t\|_2\|\vec{v}_l\|_2} \tag{11}$$

where $(\cdot)^{\mathrm{T}}$is the transposition function. Substituting (10) into (11), and assuming $\Delta\alpha$and $\Delta\gamma$ are small enough, the relationship between $\theta$and θ' can be formulated as follows:

$$\sin(\theta)=\sin(\theta')-\sin(\Delta\theta) \tag{12}$$

where

$$\begin{cases}\sin(\theta')=\sin(\alpha')\sin(\beta)\\ \sin(\Delta\theta)=\sin(\Delta\alpha)\cos(\alpha')\sin(\beta)+\sin(\Delta\gamma)\cos(\beta)\end{cases} \tag{13}$$

where $\Delta\theta$represents the included angle bias. Equation (13) indicates that the Doppler centroid of $\tilde{I}_m^0(x,y)$ is migrated with a nonideal frequency $\Delta f_{\mathrm{dc}}=2v\sin(\Delta\theta)/\lambda$. And a Doppler frequency spectrum migration is generated between subimages.

Fig. 5 depicts the influence of Δf_{dc} on the azimuth peak to side-lobe radio (PSLR) and normalized azimuth resolution of the fusion image. It indicates that the PSLR is seriously affected by the ratio of Δf_{dc} to the Doppler bandwidth B_a of the fusion image.

Besides that, $\Delta f_{\mathrm{dc}}$is space varied which means that in large sense imaging, the influence of space angle error is different. The space angle errors $(\Delta\alpha,\Delta\beta)$ need to be estimated.

To this end, a Doppler spectrum migration calibration method (DMC) is proposed. The flowchart of DMC is depicted in the inner diagram of Fig. 3. In the first step of DEC, several local images $\tilde{I}_{m,n}^0$and $I_{m+1,n}^0$ are selected. Then, the corresponding Doppler centroid $f_{m,n}$, $f_{m+1,n}$and Doppler bandwidths $B_{m,n}$, $B_{m+1,n}$ are estimated [38]–[40]. After that, the initial Doppler centroid deviation $\Delta f_{\mathrm{dc},n}$is given by

$$\Delta f_{\mathrm{dc},n}=f_{m+1,n}-f_{m,n}-\frac{B_{m,n}+B_{m+1,n}}{2}. \tag{14}$$

Considering that the estimate accuracy may be not high enough, more accurate Doppler centroid deviation is searched nearby $\Delta f_{\mathrm{dc},n}$. The searching range is set as $(-\Delta f,\Delta f)$, where $\Delta f$is the estimate accuracy of the Doppler centroid and bandwidth estimate algorithms. The search step is set as 0.5% of B_a. For different value of $\Delta f_{\mathrm{dc},n}$, $I_{m,n}^0$is reprojected and merged to $I_{m+1,n}^0$. The influence of θ'_{in} is calibrated by the phase error calibration method which is introduced in Section III-B2. After that, the fusion image $I_{m,n}^1$is obtained by adding $\tilde{I}_{m,n}^0$and $I_{m+1,n}^0$ coherently. To decide if the focus level is satisfied, the entropy of $I_{m,n}^1$is computed

$$\varepsilon\{\mathrm{I}\}=-\sum_x\sum_y\frac{\left|I_m^1(x,y)\right|^2}{E_s}\ln\frac{E_s}{\left|I_m^1(x,y)\right|^2} \tag{15}$$

where $E_s=\|I_{m,n}^1\|_2$. The Doppler centroid deviation $\Delta f_{\mathrm{dc},n}$ is obtained by achieving minimum entropy. Repeating above procedures on the local images and assume that $\mathbf{F_d}=[\Delta f_{\mathrm{dc},1},\Delta f_{\mathrm{dc},n},\ldots,\Delta f_{\mathrm{dc},N}]^T$ has been obtained. Then, based on (13), $\mathbf{F_d}$ is formulated as

$$\mathbf{F_d}=f(\boldsymbol{\alpha}',\boldsymbol{\beta})+\mathbf{e} \tag{16}$$

$$f(\boldsymbol{\alpha}',\boldsymbol{\beta})=\frac{2v}{\lambda}\left[\sin(\Delta\alpha)\cos(\boldsymbol{\alpha}')\sin(\boldsymbol{\beta})+\sin(\Delta\gamma)\cos(\boldsymbol{\beta})\right] \tag{17}$$

where $\boldsymbol{\alpha}'=[\alpha'_1,\alpha'_2,\ldots,\alpha'_N]^T$ and $\boldsymbol{\beta}=[\beta'_1,\beta'_2,\ldots,\beta'_N]^T$are the vector of the azimuth angle and look-down angle which can be calculated through the center coordinates of the imaging grids of $\tilde{I}_{m,n}^0$.$\mathbf{e}$ is the sequence of noise which be modeled as random Gaussian distribution.

In order to estimate attitude angle, based on (16), a cost function is built as

$$p(\Delta\alpha,\Delta\gamma)=\|\mathbf{F_d}-f(\boldsymbol{\alpha}',\boldsymbol{\beta})\|. \tag{18}$$

Then, the optimization problem of space angle error $(\Delta\alpha,\Delta\gamma)$is modeled as follows:

$$(\hat{\alpha},\hat{\gamma})=\underset{(\Delta\alpha,\Delta\gamma)}{\arg\min}\{p(\Delta\alpha,\Delta\gamma)\} \tag{19}$$

Least square method is a good solution to solve (19) and estimate space angle error $(\Delta\alpha,\Delta\gamma)$. After obtaining $(\Delta\alpha,\Delta\gamma)$, $\tilde{I}_m^0$is reprojected into the xy plane and merged into I_{m+1}^0. Compared to the ideal imaging result, the imaging result $\tilde{I}_m(x,y)$can be written as follows:

$$\tilde{I}_m^0(x,y)=I_m^0(x,y)\,e^{j\theta'_{\mathrm{err}}} \tag{20}$$

where $\theta_{\mathrm{err}}=\theta'_{in}-\theta_{in}$is the phase error.

3) Phase Error Calibration: An optimized method based on maximum sharpness of the image is introduced in this section to estimate θ_{err}. The discrete form of the image result I of (1) can be expressed as follows:

$$I=\sum_{n=1}^{N}b_n,n=1,2,3\ldots,N \tag{21}$$

where $b_n=s(a_n,r)\mathrm{e}^{j\frac{4\pi r}{\lambda}}$ is the BPA image of each azimuth sample. Considered the phase error φ_n , (21) can be rewritten as follows:

$$\tilde{I}=\sum_{n=1}^{N}\tilde{b}_n \tag{22}$$

where $\tilde{b}_n = b_n e^{j\varphi_n}$, and $\tilde{I}$is the defocused image. The objective of the autofocus method is to estimate phase errors $\hat{\varphi}= \{\hat{\varphi}_1, \hat{\varphi}_2, \ldots, \hat{\varphi}_N\}$ and compensate the phase errors to the defocused image $I = \sum_{n=1}^{N} \tilde{b}_n e^{-j\hat{\varphi}_n}$. The image sharpness $\Xi = \|I\|_2$ is modeled as a function of the phase error$\hat{\varphi}$. As is known, the more accurate the estimated phase error, the larger value the image sharpness. Thus, the optimal correction phase factor is

$$\hat{\varphi} = \arg\max \Xi(\hat{\varphi}) \tag{23}$$

rearrange (22) to (24), we obtain

$$\tilde{I} = q + pe^{-j\hat{\varphi}_{n_0}} \tag{24}$$

where

$$\begin{cases} q = \sum\limits_{1}^{n_0-1} \tilde{b}_n e^{-j\hat{\varphi}_n} + \sum\limits_{n_0+1}^{N} \tilde{b}_n e^{-j\hat{\varphi}_n} \\ p = \tilde{b}_{n_0} \end{cases}. \tag{25}$$

Then the intensity of parameters in $\tilde{I}$ can be expressed as follows:

$$\Upsilon_i = \tilde{I}_i^2 = \underbrace{|q_i|^2 + |p_i|^2}_{(\Upsilon_0)_i} + \underbrace{\Re(q_i {p_i}^* e^{j\hat{\varphi}_n})}_{(\Upsilon_1)_i} \tag{26}$$

where $\Re(\cdot)$ means real part; "$*$" is the conjugate operation. In vector form, the intensity image may be written as$\Upsilon = \Upsilon_0 + \Upsilon_1$. To solve the problem of (26), coordinate descent (CD) is an alternative solution [32]. In this article, after PGA and registration, we rewrite (22) as

$$\tilde{I} = \tilde{I}_m^0 + I_{m+1}^0. \tag{27}$$

The objective of (27) is to estimateθ_{err} , which has the similar optimal function of (23). It is also noted that the $q$in (24) is to provide priori information of imaging position and preliminary imaging results of the target. After previous processing, $\tilde{I}_m^0$ can provide that priori knowledge independently. Thus, CD can be applied in $\tilde{I}_m^0$ and I_{m+1}^0 to estimate and calibrate the phase error. After that well-focused imaging can be obtained by accumulate subimages coherently. Moreover, if the frequency gap can be ignored, MFGA can be simplified by ignoring DMC. Image registration can be applied in all subimages first and CD can be optimized to Fast CD (FCD) by using base-2 image merging

$$\begin{cases} I_m^{(k+1)} = \mathcal{F}\left(I_{2m-1}^{(k)}, I_{2m}^{(k)}\right) \\ q = I_{2m-1}^{(k)} \\ p = I_{2m}^{(k)} \end{cases} \tag{28}$$

where $I_m^{(k+1)}$means the mth image fusion result in $(k+1)$th level; $\mathcal{F}(\cdot)$ means CD method.

MFGA is effective and efficient for WA-SAR image with time delay error. It keeps the time efficiency of FFBP and PGA. Compared with the traditional methods [27]–[31] which are based on image quality evaluation criterion, MFGA has less iteration. The iteration times are reduced from the number of azimuth pulse to the number of subimages. Besides that, base-2 image fusion allows implementation of parallel processing which also accelerates the imaging procedure. Compared to FGA, MFGA divided the influence into three individual categories and calibrate those influences independence. Thus, MFGA can avoid the tremendous time consumption of parameters searching in FGA. The flowchart of the proposed method is described in detail as follows.

1) The defocused subimages $I_m^0(r', \tilde{k}'_\Omega)$ in ground virtual polar coordinates are obtained by FFBP.
2) Well focused sub-images $I_m^0(r', \tilde{k}'_\Omega)$ are obtained through PGA.
3) ObtainI_m^1 by implement MFGA on I_m^0 and I_{m+1}^0.
4) Update sub-images and repeat step 3) until one full-resolution image left.

In Section IV, the processing results of numerical simulation and real SAR data experiments are given to verify the effectiveness of MFGA.

TABLE I
SIMULATION AND REAL DATA PARAMETERS

	Data set 1	Data set 2	Data set 3
SAR mode	Stripmap	Stripmap	Stripmap
Centre frequency	1.3GHz	1.3GHz	1.3GHz
Bandwidth	200MHz	200MHz	200MHz
PRF	1000Hz	1000Hz	1000Hz
Designed azimuth angle	0°	0°	0°
Actual azimuth angle	5°(average)	17°(average)	7°(average)
Size of scene	9km*6km	9km*6km	9km*6km
Platform	Helicopter	Helicopter	Airship
Velocity	25m/s	25m/s	25m/s
Azimuth beamwidth	30°	30°	30°

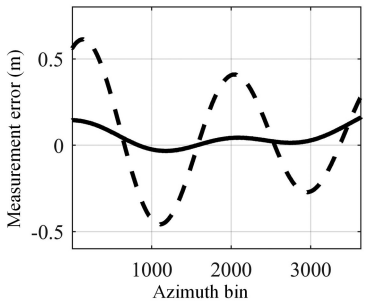

Fig. 6. Trajectory deviation, solid line: data set 1; dotted line: dataset 2.

IV. EXPERIMENTS

A. Numerical Simulation

Simulated data are generated in stripmap mode with ideal straight line by the system parameters shows in Table I dataset 1 and imaged with different system calibration error and trajectory deviation.

1) Dataset 1: In dataset 1, the echo of 25 isolate points (5×5) is generated. Small trajectory deviation, as shown in the solid line of Fig. 6, is added into the flight track. For comparison, FGA, FFBP autofocus [34], and MFGA are used to obtain the SAR images, respectively.

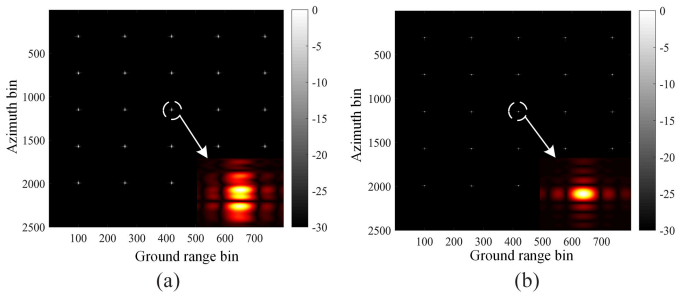

Fig. 7. Simulation results by using FFBP and MFGA. (a) defocused image with FFBP (b) focused image with MFGA.

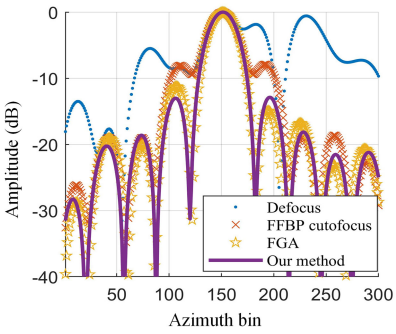

Fig. 8. Azimuth profiles of the center point target of multiple methods.

Fig. 7 displays the simulation results. Fig. 7(a) and (b) show us the imaging results by FFBP and the MFGA, respectively. To further specify the focusing performance, Fig. 8 shows us the azimuth profile of the center point by different methods. The processing results of FFBP without the motion compensation, FFBP focus [28], FGA and the MFGA are shown in Fig. 8. Comparing the results of FFBP autofocus method, FGA and the proposed method, we can see that the peak side lobe ratios (PSLR) are –7.91, –11.23, and –13.01 dB, respectively. The side-lobe obtained by FGA is asymmetric which shows us that MFGA has better performance than other methods.

2) Dataset 2: In dataset 2, larger trajectory deviation, as shown in the dotted line of Fig. 6, is added into the flight track to simulate space angle error. The maximum measurement error is up to 0.6 m. Caused by the large trajectory deviation, the maximum percentage of spectrum migration is up to 5%. Moreover, a 30 m range calibration error is brought in. Fig. 9 gives the imaging result of FFBP. It can be seen that caused by large trajectory deviation and range calibration error, the imaging result is defocused and all the energy spread in a large area. For comparison, ASH [30] and MFGA are implemented. The imaging results are shown in Fig. 10. Affected by the non-negligible RCM error, the imaging result of ASH is focused into three scatters. On the contrary, by combining sub-images merging, the influence of RCM is avoided and the raw data is well-focused by MFGA as shown in Fig. 10(b).

To demonstrate the importance of DMC, Fig. 11 gives the azimuth profiles of the proposed algorithm with/without applying DMC (dotted/solid line). Under applying DMC, the PSLR

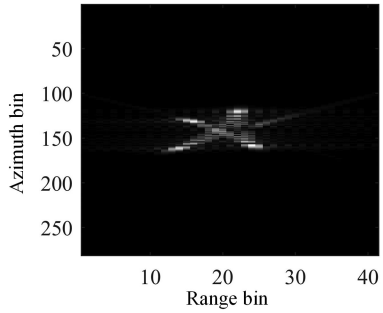

Fig. 9. Defocused image by FFBP.

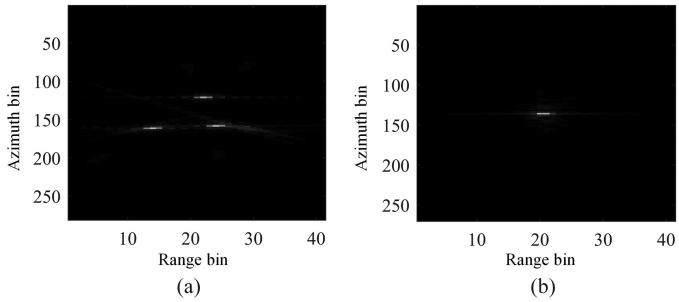

Fig. 10. Imaging results by (a) ASH and (b) proposed imaging algorithm.

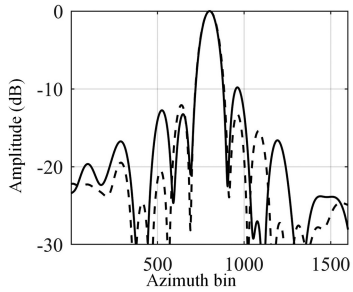

Fig. 11. Azimuth profiles of target of MFGA. Solid line: without DMC; dotted line: with DMC.

of imaging result is optimized from –9.808 to –12.882 dB. Numerical simulation shows that MFGA has better performance on FFBP image autofocus with large time delay error and the trajectory deviation.

B. Real Data Processing

Series airborne experiments are carried out in Hebei province, China. The parameters of the high-resolution WA-SAR system are shown in Table I. Slow speed platforms (helicopter and airship) are chosen as SAR carrier. As light and low speed platform, the motion of radar platform is unstable and seriously affected by the environment. Fig. 12 shows us part of the measured data of the helicopter motion state (dataset 2 of Table I). Fig. 12(a) is the measured flight track and Fig. 12(b) is the measured azimuth angle. As we can see, the azimuth angle is varied from 5° to 25° and the measured motion curve is way from a straight line. Furthermore, the vibration of the helicopter's propeller will be

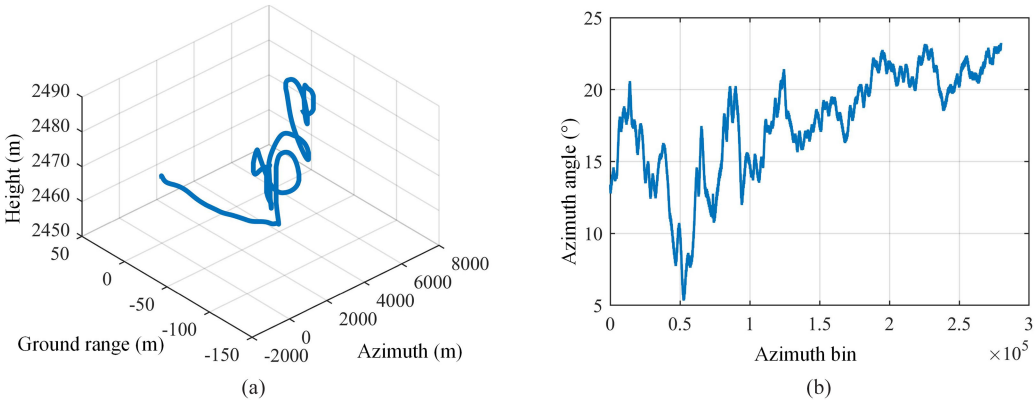

Fig. 12. Trajectory and azimuth angle of Radar platform. (a) Time varied trajectory. (b) Time varied azimuth angle.

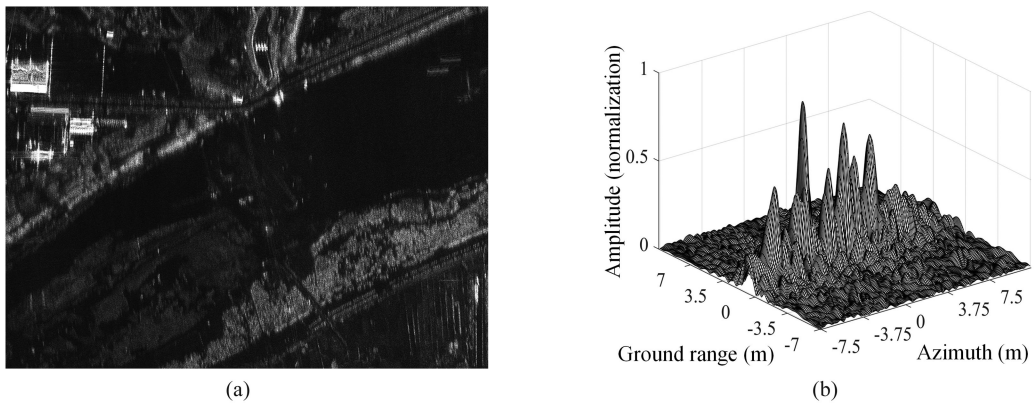

Fig. 13. Defocused image by FFBP without autofocus. (a) Image result of target sense. (b) Mesh plot of trihedral.

TABLE II
COMPUTER CONFIGURATION AND DATA VOLUME

Computer processing unit (CPU)	E4-2690 v4
CPU Frequency	2.6GHz
Memory	192GB
Data volume	7.9GB
Sampling number in azimuth	10^5
Processing language	MATLAB

TABLE III
IMAGE RESULT WITH DIFFERENT AUTOFOCUS METHOD

	FGA	ASH	Proposed method
PSLR	-4.33dB	-15.62dB	-16.71dB
Azimuth resolution	0.2392m	0.2588m	0.2624m
Time consumption	~	86135.2s (206×26 pixels)	72.76s (3900×2487 pixels)

transferred to radar sensors and bring high-frequency motion components which cannot be measured accurately and timely with the low sampling rates of IMU and GPS.

Three datasets obtained by helicopter and airship under different circumstances are processed by MFGA. Although the designed parameters of dataset 1 and dataset 2 are the same, the data acquisition geometry is different under the complicated environment. The average squint angle of data set 1 and data set 2 corresponds to 4° and13° respectively. Fortunately, the proposed method can be conveniently used to improve the focusing performance even though the SAR system works in squint geometry. To prove the performance of the refocused image, a trihedral is put in the scene. The real data is processed in the same computer configuration. Table II shows the computer configuration and data volume.

The echoes are focused in the ground plane whose horizontal axis and the vertical axis are represent the ground range direction and the azimuth direction, respectively. Fig. 13(a) is the defocused imaging result by FFBP of dataset 1. The mesh plot of trihedral is shown as Fig. 13(b). Fig. 14(a) is the focused image result by FGA of dataset 1. The mesh plot of trihedral is shown as Fig. 14(b). Fig. 15(a) is the focused image result by MFGA of data set 1. The mesh plot of trihedral is shown as Fig. 15(b). The azimuth profiles of defocused imaging result and focused imaging result by ASH [32], FGA and MFGA are shown in Fig. 16. Table III shows the imaging performance of

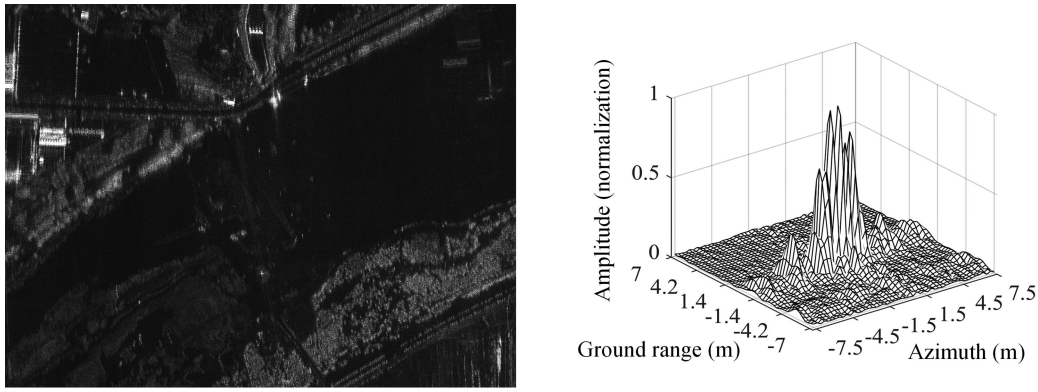

(a) (b)

Fig. 14. Refocused imaging result by FGA. (a) Image result of target sense. (b) Mesh plot of trihedral.

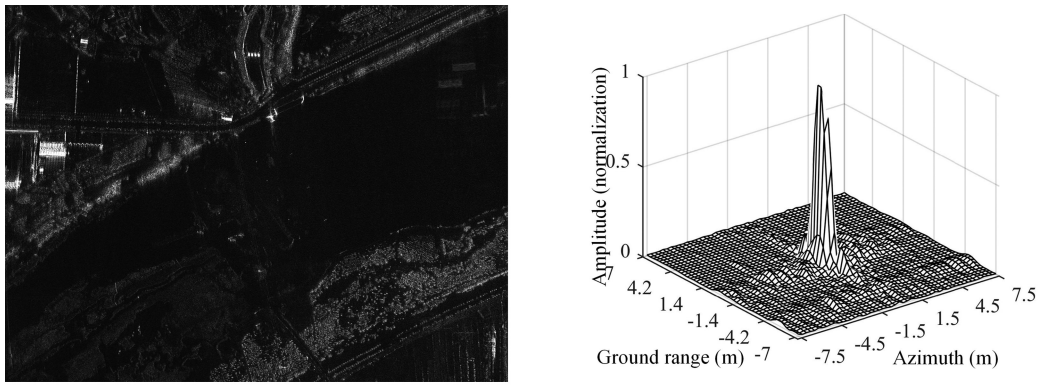

(a) (b)

Fig. 15. Refocused imaging result by MFGA. (a) Image result of target sense. (b) Mesh plot of trihedral.

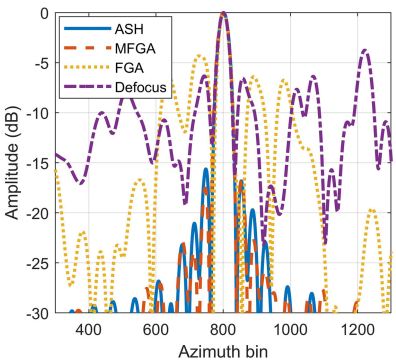

Fig. 16. Azimuth profile of trihedral of FFBP and multiple autofocus methods.

different autofocus methods. For the defocused image and FGA, the azimuth profiles of trihedral are split into several peaks. The PSLR of ASH and MFGA is –15.62 and –16.71 dB. The side lobe of ASH is asymmetric. Azimuth resolution is 0.2588 and 0.2624 m. The result shows that the proposed method has close focusing performance with ASH than other methods. Because of the huge azimuth sampling number, the time consumption for part of target sense (about 206 pixels in azimuth plus 26 pixels in range) by ASH is almost 86135.2 s. Besides that, because of the lack of consideration of image distortion and RCMC error, parallel processing cannot be introduced to ASH. On the contrary, by utilizing parallel proposing and subimages autofocus, the imaging time of MFGA for larger scene (about 3900 pixels in azimuth plus 2487 pixels in range) is only 72.76 s. Compared to FGA, MFGA considered phase and spectrum consistency between subimages. The imaging time of FGA has not been discussed because of the disgusting image performance.

Fig. 17 depicts the image result of dataset 2. Fig. 17(a) is the defocused image and Fig. 17(b) is focused image by MFGA. Fig. 18is the image result of dataset 3 which is obtained by airship which has similar motion state with helicopter. Fig. 18(a) is the defocused image and Fig. 18(b) is focused image by MFGA.

To verify the SAR imaging quality, image entropy is chosen as an evaluation criterion, which represents the randomness of the SAR images. The smaller the entropy is, the better quality of the image is.

Table IV shows the image entropy of image results of dataset 2 and dataset 3. Table IV demonstrates that MFGA is also suitable for squint SAR and any other platform.

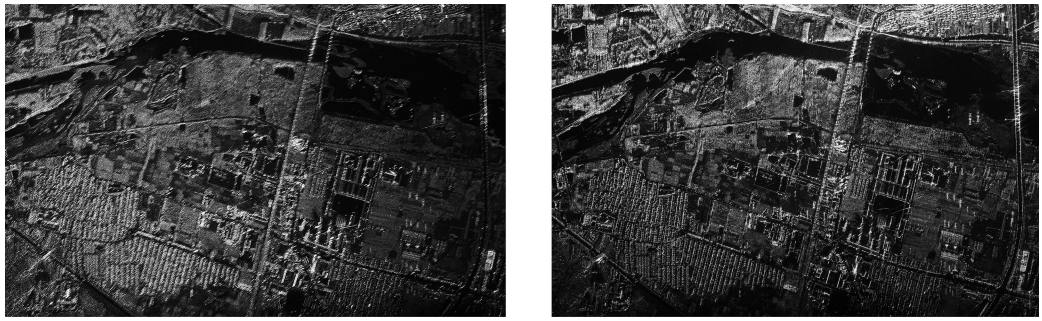

(a) (b)

Fig. 17. Imaging result. (a) Defocused image by FFBP. (b) Focused image by MFGA.

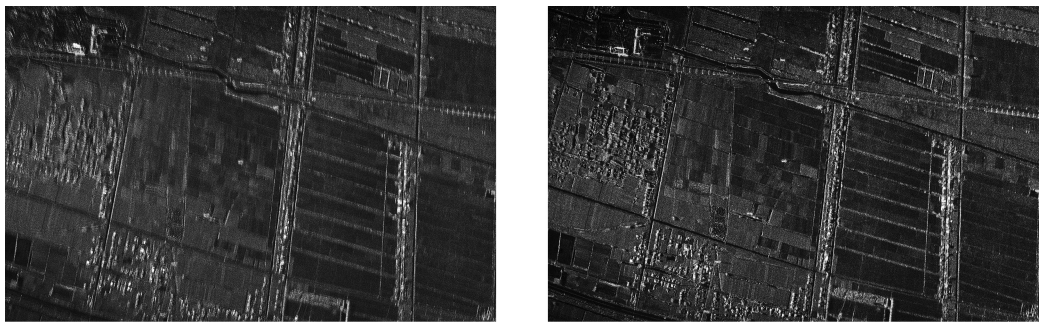

(a) (b)

Fig. 18. Imaging result. (a) Defocused image by FFBP. (b) focused image by MFGA.

TABLE IV
IMAGE ENTROPY OF IMAGE RESULT

	Data set 2	Data set 3
Without autofocus	16.27	15.64
Proposed method	15.51	14.92

V. CONCLUSION

In this article, we proposed a geometrical autofocus algorithm combing PGA for WA-SAR. We formulated factorized geometrical error into three independent factors: image distortion, spectrum migration, and the phase error. By compensating such factors in the different signal domains, we can correct the discontinuous signal between subimages caused by motion statement error and time delay error. Besides, our proposed algorithm can also avoid the time-consuming geometric parameters searching in the traditional FGA. To conclude, MFGA is effective and efficient in compensating RCMC error for WA-SAR.

Autofocus imaging experiments on simulated and real data show that MFGA performs exceptionally and applies to multiple SAR modes such as strip-map SAR and squint SAR in different unstable platform with less computational complexity and memory consumption. Moreover, we can extend MFGA for bistatic SAR systems by considering additional system calibration error.

REFERENCES

[1] C. A. Wiley, "Synthetic aperture radars," *IEEE Trans. Aerosp. Electron. Syst.*, vol. AES-21, no. 3, pp. 440–443, May 1985.
[2] I. Cumming and J. Bennett, "Digital processing of seasat SAR data," in *Proc. IEEE Int. Conf. Acoust., Speech, Signal Process.*, 1979, pp. 710–718.
[3] W. Tang *et al.*, "High-resolution SAR altimeter with wide-angle echoes coherent accumulation," *J. Eng.*, vol. 2019, pp. 8142–8145, 2019.
[4] J. Ash *et al.*, "Wide-Angle synthetic aperture radar imaging: Models and algorithms for anisotropic scattering," *IEEE Signal Process.*, vol. 31, no. 4, pp. 16–26, Jul. 2014.
[5] C. Sun, Q. Chang, and Y. Wang, "Wide-angle SAR imaging based on sub-apertures joint sparse reconstruction," in *Proc. IEEE MTT-S Int. Wireless Symp.*, May 2018, pp. 1–3
[6] R. Bamler, "A comparison of range-Doppler and wavenumber domain SAR focusing methods," *IEEE Trans. Geosci. Remote Sens.*, vol. 30, no. 4, pp. 706–713, Jul. 1992.
[7] R. K. Raney, H. Runge, R. Bamler, I. G. Cumming, and F. H. Wong, "Precision SAR processing using chirp scaling," *IEEE Trans. Geosci. Remote Sens.*, vol. 32, no. 4, pp. 786–799, Jul. 1994.
[8] J. L. Walker, "Range-Doppler imaging of rotating objects," *IEEE Trans. Aerosp. Electron. Syst.*, vol. AES-16, no. 1, pp. 23–52, Jan. 1980.
[9] J. W. Mccorkle, "Focusing of synthetic aperture ultra wideband data," in *Proc. IEEE 1991 Int. Conf. Syst. Eng.*, 1991, pp. 1–5
[10] A. F. Yegulalp, "Fast back-projection method for synthetic aperture radar," in *Proc. IEEE Radar Conf.. Radar into Next Millennium*, 1999, pp. 60–65.
[11] S. Xiao *et al.*, "An N^2logN back-projection method for SAR image formation," in *Proc. Conf. Rec. 34th Asilomar Conf. Signals, Syst. Comput.*, 2000, vol. 1, pp. 3–7.
[12] L. M. H. Ulander, H. Hellsten, and G. Stenstrom, "Synthetic-aperture radar processing using fast factorized back-projection," *IEEE Trans. Aerosp. Electron. Syst.*, vol. 39, no. 3, pp. 760–776, Jul. 2003.

[13] M. Rodriguez-Cassola, P. Prats, G. Krieger, and A. Moreira, "Efficient time-domain image formation with precise topography accommodation for general bistatic sar configurations," *IEEE Trans. Aerosp. Electron. Syst.*, vol. 47, no. 4, pp. 2949–2966, Oct. 2011.
[14] H. L. Li *et al.*, "Innovative strategy for stripmap SAR imaging using fast factorized back-projection," *J. Electron. Inf. Technol.*, vol. 37, no. 8, pp. 1808–1813, 2015.
[15] P. Thompson *et al.*, *Spotlight-Mode Synthetic Aperture Radar: A Signal Processing Approach*. New York, NY, USA: Springer, 1996, pp. 330–332.
[16] W. G. Carrara, R. S. Goodman, and R. M. Majewski, "Spotlight synthetic aperture radar: Signal processing methods," *J. Atmospheric Sol.-Terrestrial Phys.*, vol. 59, no. 5, pp. 597–598, 1995.
[17] D. Zhu, R. Jiang, X. Mao, and Z. Zhu , "Multi-sub aperture PGA for SAR autofocusing," *IEEE Trans. Aerosp. Electron. Syst.*, vol. 49, no. 1, pp. 468–488, Jan. 2013.
[18] Z. Lu, Z. Ding, T. Long, and L. Chen, "A novel autofocusing technique based on PGA for the polarimetric SAR application," in *Proc. IEEE Int. Geosci. Remote Sens. Symp.*, 2012, pp. 5872–5875
[19] Y. Tang *et al.*, "The space-variant phase-error matching map-drift method for highly squinted SAR," *IEEE Geosci. Remote Sens. Lett.*, vol. 10, no. 4, pp. 845–849, Jul. 2013.
[20] O. O. Bezvesilniy, I. M. Gorovyi, and D. M. Vavriv, "Estimation of phase errors in SAR data by local-quadratic map-drift autofocus," in *Proc. 13th Int. Radar Symp.*, 2012, pp. 376–381.
[21] D. E. Wahl, P. H. Eichel, D. C. Ghiglia, and C. V. Jakowatz, "Phase gradient autofocus-a robust tool for high resolution SAR phase correction," *IEEE Trans. Aerosp. Electron. Syst.*, vol. 30, no. 3, pp. 827–835, Jul. 1994.
[22] L. Zhang, H.-L. Li, Z.-J. Qiao, M.-D. Xing, and Z. Bao, "Integrating autofocus techniques with fast factorized back-projection for high-resolution spotlight SAR imaging," *IEEE Geosci. Remote Sens. Lett.*, vol. 10, no. 6, pp. 1394–1398, Nov. 2013.
[23] C. V. Jakowatz and N. Doren, "Comparison of polar formatting and back-projection methods for spotlight-mode SAR image formation," *Proc. SPIE*, vol. 6237, 2006, Art. no. 62370H. doi: 10.1117/12.673249.
[24] F. D. Garber, "Considerations for autofocus of spotlight-mode SAR imagery created using a beamforming method," *Proc. SPIE*, vol. 7337, 2009, Art. no. 73370A. doi: 10.1117/12.820049.
[25] J. Torgrimsson, P. Dammert, H. Hellsten, and L. M. H. Ulander., "SAR processing without a motion measurement system," *IEEE Trans. Geosci. Remote Sens.*, vol. 57, no. 2, pp. 1025–1039, Feb. 2019.
[26] J. Torgrimsson, P. Dammert, H. Hellsten, and L. M. H. Ulander, "Factorized geometrical autofocus for synthetic aperture radar processing," *IEEE Trans. Geosci. Remote Sens.*, vol. 52, no. 10, pp. 6674–6687, Oct. 2014.
[27] Y. Luo, F. Zhao, N. Li, and H. Zhang, "An autofocus cartesian factorized back projection method for spotlight synthetic aperture radar imaging," *IEEE Geosci. Remote Sens. Lett.*, vol. 15, no. 8, pp. 1244–1248, Aug. 2018.
[28] L. Ran, Z. Liu, T. Zhang, and T. Li, "Autofocus for correcting three dimensional trajectory deviations in synthetic aperture radar," in *Proc. CIE Int. Conf. Radar*, 2016, pp. 1–4.
[29] K. Hu, X. Zhang, S. He, H. Zhao, and J. Shi, "A less-memory and high-efficiency autofocus back projection method for SAR imaging," *IEEE Geosci. Remote Sens. Lett.*, vol. 12, no. 4, pp. 890–894, Apr. 2015.
[30] J. N. Ash, "An autofocus method for back projection imagery in synthetic aperture radar," *IEEE Geosci. Remote Sens. Lett.*, vol. 9, no. 1, pp. 104–108, Jan. 2012.
[31] L. Chen, D. An, and X. Huang, "Extended autofocus back projection method for low-frequency SAR imaging," *IEEE Geosci. Remote Sens. Lett.*, vol. 14, no. 8, pp. 1323–1327, Aug. 2017.
[32] J. Wu, Y. Li, W. Pu, Z. Li, and J. Yang, "An effective autofocus method for fast factorized back-projection," *IEEE Trans. Geosci. Remote Sens.*, vol. 57, no. 8, pp. 6145–6154, Aug. 2019.
[33] Y. Li *et al.*, "An autofocus method based on maximum image sharpness for fast factorized back-projection," in *Proc. IEEE Radar Conf.*, 2017, pp. 1201–1204.
[34] J. Wang *et al.*, "ISAR minimum-entropy phase adjustment," in *Proc. IEEE Radar Conf.*, 2004, pp. 197–200.
[35] L. Xi, G. Liu, and J. Ni, "Autofocusing of ISAR images based on entropy minimization," *IEEE Trans. Aerosp. Electron. Syst.*, vol. 35, no. 4, pp. 1240–1252, Oct. 1999.
[36] H. Lu *et al.*, "InSAR baseline estimation for Gaofen-3 real-time DEM generation," *Sensors*, vol. 18, no. 7, 2018, Art. no. 2152.
[37] N. Cao *et al.*, "Estimation of residual motion errors in airborne SAR interferometry based on time-domain back projection and multisquint techniques," *IEEE Trans. Geosci. Remote Sens.*, vol. 56, no. 4, pp. 2397–2407, Apr. 2018.
[38] T. Long, Z. Lu, Z. Ding, and L. Liu, "A DBS doppler centroid estimation algorithm based on entropy minimization," *IEEE Trans. Geosci. Remote Sens.*, vol. 49, no. 10, pp. 3703–3720, Oct. 2011.
[39] R. Bamler, "Doppler frequency estimation and the cramér–rao bound," *IEEE Trans. Geosci. Remote Sens.*, vol. 29, no. 3, pp. 385–389, May 1991.
[40] X. Huang *et al.*, "A fast algorithm of LFM signal detection and parameter estimation based on efficient FrFT," *J. Electron. Inf. Technol.*, vol. 39, no. 12, pp. 2905–2911, 2017.

Han Li was born in Jiangxi, China, in May 1993. He received the B.Eng. degree in electrical engineering from Xidian University, Xi'an, China, in 2015. He is currently working toward the Ph.D. degree with the National Key Laboratory of Radar Signal Processing, Xidian University.

His research interests include multichannel SAR imaging and Doppler parameter estimation.

Zhiyong Suo was born in Lingshou, Hebei, China, in 1979. He received the B.S. degree in electronic information engineering and the Ph.D. degree in signal and information processing, from Xidian University, Xi'an, China, in 2003 and 2009, respectively.

Since 2010, he has been an Associate Professor with the National Laboratory of Radar Signal Processing, Xidian University. His main research interests include SAR imaging, radar system design, signal processing and application of InSAR, DInSAR, and PolInSAR.

Chengxin Zheng was born in Shandong, China, in April 1994. She received the B.Eng. degree in electrical engineering from Qingdao University, Qingdao, China, in 2017, and the M.S. degree in electronic information engineering from Xidian University, Xi'an, China, in 2020.

Her research interests include multichannel SAR imaging and Doppler parameter estimation.

Zhenfang Li received the B.S. degree in automatization and the M.S. degree in electronic information engineering from Xidian University, Xi'an, China, in 1999 and 2001, respectively, and the Ph.D. degree in radar signal processing from the National Laboratory of Radar Signal Processing, Xidian University, in 2006.

He was an Associate Professor with the National Laboratory of Radar Signal Processing, Xidian University, in 2006–2010. Since 2010, he has been a Professor with the National Lab. of Radar Signal Processing, Xidian University. His current research interests include SAR and GMTI signal processing of distributed small satellite SAR systems.

Bingji Zhao received the B.S. degree in electronic engineering and information science from the Ha'er Bin Engineering University, Heilongjiang, China, in 2007, and the Ph.D. degree in communication and information system from the Institute of Electronics, University of Chinese Academy of Science, Beijing, China, in 2013.

In 2013, he joined the Beijing Institute of Spacecraft System Engineering in CAST, where he was currently funded by "Outstanding Young Scientists in CAST." He is currently a Senior Engineer and has been the Technical Director of several spaceborne SAR satellite and one airborne SAR programs. His current research interests include geosynchronous synthetic aperture radar (Geo-SAR) and Low Earth orbital high- resolution Spaceborne SAR system designing and 3-D SAR imaging techniques.